Retrieval of Precipitation from Microwave Airborne Sensors during TOGA COARE

NICOLAS VILTARD, ESTELLE OBLIGIS, VIRGINIE MARECAL, AND CLAUDE KLAPISZ

Centre d'Etude des Environnements Terrestre et Planétaires, CNRS–Université de Versailles Saint-Quentin, Velizy, France

(Manuscript received 14 January 1997, in final form 24 June 1997)

ABSTRACT

The aim of this paper is to report on the retrieval of the vertically averaged liquid cloud water content and vertically averaged precipitation rates (rain and ice) from microwave airborne radiometric observations in a two-plane parallel layer atmosphere. The approach is based on the inversion of a simple radiative transfer model in which a raindrop size distribution derived from microphysical measurements is introduced. The microwave data (18.7, 21, 37, and 92 GHz) used were acquired by the Airborne Multichannel Microwave Radiometer and Advanced Microwave Moisture Sounder on board NASA DC8 within a mesoscale convective system on 6 February 1993 during the Tropical Oceans Global Atmosphere Coupled Ocean–Atmosphere Response Experiment.

Before interpreting the results, the quality of the inversion is checked. The fit between the measured and the model-retrieved brightness temperatures is good when compared to the model and measurements uncertainties. Doppler radar data from three other aircraft help the result's interpretation, providing reflectivity and wind fields. The cloud liquid content seems to be difficult to retrieve. The ice and liquid rain rates are consistent with the other data sources: order of magnitude for convective and stratiform regions, presence of ice and liquid precipitation correlated with cell structure, and presence of cloud particles in the lighter precipitating regions.

A quantitative comparison is done between the radiometric rainfall rates and those derived from the Airborne Rain Mapping Radar observations (also on board NASA DC8). There is a good agreement between the two from the statistical point of view (mean and standard deviation values). Moreover, the finescale rain structures that appear in radar results are rather well reproduced in the radiometric results. The importance of the new drop size distribution introduced in the radiative transfer model is emphasized by this last comparison.

1. Introduction

During 1997, the Tropical Rain Measuring Mission (TRMM) satellite was launched. For the very first time, a rain radar and a radiometer will take measurements from space in the tropical regions. These instruments will provide a very powerful tool to estimate the precipitation over these zones covered at least 75% by oceans. To prepare for this mission, the National Aeronautics and Space Administration (NASA) equipped an aircraft during TOGA COARE (Tropical Oceans Global Atmosphere Coupled Ocean–Atmosphere Response Experiment) with a passive radiometer and a radar in a configuration close to that of TRMM (Simpson et al. 1988).

The remote sensing techniques for precipitation that use passive microwaves are usually separated in three classes that may be used depending on the considered problem. First, the statistical–empirical methods consist of using a regression between observed radiance and ground-based measurements considered as the ''truth.'' These algorithms are based on the lowest frequency and the emission/absorption effect by raindrops (Wilheit et al. 1991; Hinton et al. 1992; Petty and Katsaros 1992; Prabhakara et al. 1992) or on an indirect relation between rain rate and ice scattering (Spencer et al. 1989; Grody 1991; Adler et al. 1991) or take into account both emission and scattering (Liu and Curry 1992; Adler et al. 1993). These methods are easy and computationally efficient but have to be considered with extreme caution when applied to another dataset in another climatic situation. Second, the physical methods use a set of theoretically established relationships between brightness temperatures (hereafter T_B) and precipitation. These last methods are based on a radiative transfer model (hereafter RTM) that necessarily contains some assumptions about the structure of the atmosphere and its interactions with the microwaves. On the other hand, this representation of the physics leads to a better understanding of the involved phenomena and thus the different assumptions may be included directly by modifications in the model. Third, the mixed statistical–physical methods use a mesoscale cloud model and a radiative transfer model to build a database of profiles of atmospheric variables associated with emerging brightness temper-

Corresponding author address: Dr. Nicolas Viltard, CETP, 10–12 avenue de l'Europe, 78140 Vélizy, France.
E-mail: viltard@cetp.ipsl.fr

atures. The retrieval consists in finding the realistic mean atmospheric profile in the database while using a dataset of measured brightness temperature as input (see Smith et al. 1992; Mugnai et al. 1993; Kummerow and Giglio 1994a,b; Kummerow et al. 1996).

In this paper, we are more interested in the second method. While remaining easy to use, it allows us to understand the physics underlying the retrieval. The TOGA COARE experiment offers a very favorable frame for our purpose because several mesoscale convective systems were sampled simultaneously by very different and complementary instruments. In this experiment, the airborne radiometers were operated in order to develop and/or to improve radiometric retrieval of precipitation for the future spaceborne TRMM mission. Airborne data present an intrinsic advantage because of the pixel size. It is about 1 km at nadir, which is much smaller than the horizontal size of the convective cells, typically about 3–5 km. Thus, the problem of pixel inhomogeneity is minimized with respect to satellite data.

In this context our main objective was to test a simple method to retrieve the cloud and precipitation spatial distribution based on a numerical inversion of a radiative transfer model. Application to the datasets of the 6 February 1993 TOGA COARE mission provides a unique opportunity to study the reliability of the results using comparison with information from other data sources. Evidence of the interest of such an approach is also given in McGaughey and Zipser (1996a), where a radiometric dataset from the Advanced Microwave Precipitation Radiometer (aboard NASA ER2) is analyzed with the support of three-dimensional reflectivity fields deduced from radars aboard other aircraft. In the present study, the first step was to use reflectivity and wind fields deduced from aircraft Doppler 10-GHz radar to check the consistency of the radiometric retrieved variables. The second step was to perform a quantitative comparison between the liquid rain rate retrieved from radiometric data and from the 13.8-GHz radar data aboard the same platform.

In section 2, a brief presentation of the 6 February 1993 case allows us to describe both the instrumental context and the large-scale situation and to introduce the mesoscale convective system observed during this mission. The DC8 radar and radiometric datasets are more precisely presented in section 3, with a description of the different precipitation structures that may be distinguished at meso- to small scale. In section 4, the basics of the radiative transfer model and its numerical inversion are explained. Section 5 presents the arguments used to qualify the inversion. The results are also discussed in this section with respect to comparisons with radar data. Section 6 gives the conclusions of the present study.

2. The case of 6 February 1993

The TOGA COARE experiment was conducted from November 1992 through February 1993 to describe the processes responsible for the strong coupling between the ocean and the atmosphere in the western Pacific warm pool and its effects on the global climate (Webster and Lukas 1992). It took place between 10°N and 10°S and 140°E and the date line. This tropical region was chosen because it contains the warmest ocean water, it is frequently disturbed by convective systems, and it receives a great amount of precipitation.

In the whole observation set of the TOGA COARE campaign, the 6 February 1993 case was selected because it was a well-sampled system fully explored by four of the aircraft involved in the experiment: first, the two National Oceanic and Atmospheric Administration (NOAA) P3s were equipped with Doppler 10-GHz radar and flew parallel tracks, respectively, in front of and in back of the line; second, the National Center for Atmospheric Research (NCAR) Electra flew some crossline legs, at about 3-km altitude, providing both Doppler radar data and microphysical measurements. Finally, the NASA DC8 flew alongline tracks sampling the system with radar and microwave radiometers that are described in section 3.

Figure 1 presents the infrared pictures viewed by Operational Linescan System on board a Defense Meteorological Satellite. The large-scale situation was mainly under the influence of Tropical Cyclone Oliver (lower left corner of the Fig. 1) over the Solomon Sea. Two organized large-scale cloud bands on the northern side of Oliver can also be seen. The first one was the closest to the center of the cyclone and it originated from Papua, New Guinea; the second one turned northeast over the Solomon Islands. Over these bands, the low infrared temperatures observed indicate high-altitude cloud tops that usually characterize convection. The mesoscale convective system (MCS) sampled by the aircraft is part of the first band at about 700 km from Oliver's eye (Fig. 1). The DC8 flight track is also shown in Fig. 1 with respect to the systems.

Using the Doppler tail radars, data from both NOAA and NCAR aircraft and information about the kinematics and microphysics of the MCS may be deduced. Two half-hour composites of the reflectivity fields at 3-km altitude are presented in Fig. 2a (1600–1630 UTC) and Fig. 2b (1800–1830 UTC), in 200 km × 200 km domains, with 2-km horizontal resolution. These composites are obtained by maximizing the reflectivity measured by the three aircraft at every grid point during the considered half-hour. The structures of maximum reflectivity (greater than 27 dBZ) are elongated toward the southeast, which is approximately the direction of propagation of the system (toward 120° at about 6 m s^{-1}). For the first composite (1600–1630 UTC), Doppler information (not displayed here) shows evidence in the atmospheric low levels of strong convergence between northwest and northeast winds that meet along the direction of extension of the line. This convergence induces updrafts that generate the most intense precipitating regions (referred to as ''convective line'') pointed

out by reflectivity values greater than 27 dBZ (absolute maximum reflectivity of Fig. 2a is 41.2 dBZ). The second composite (1800–1830 UTC) presents a less elongated structure of reflectivity values greater than 27 dBZ (absolute maximum reflectivity of Fig. 2b is 41 dBZ). At this time, the low-level northwest wind is weaker than previously reported, and the northeast wind is stronger. The upper-level wind (9-km altitude) evolves during the same time interval, shifting from northwesterlies at 1600–1630 to westerlies at 1800–1830. This evolution may explain the eastward extension of the convective line when looking at the second composite (Fig. 2b). A more detailed description of the structure and evolution of this shear parallel line can be found in Roux et al. (1996).

During the DC8 flight, five distinct legs have been selected for their interest. The trajectories are presented in Figs. 2a and 2b, superimposed with the reflectivity fields previously described. Note that the collocation of the DC8 position over the P3 and Electra's reflectivity field is done at about 5-km accuracy, due to composition of half an hour of advected data and the accuracy of navigation systems aboard the aircraft. The data were collected all along the MCS main horizontal extension during these legs and will present a variety of different situations within the system.

3. Datasets

The aircraft data used to retrieve the considered atmospheric variables were obtained from radiometers flown aboard the DC8 aircraft. The aircraft altitude was between 9.5 and 10.5 km and its velocity was about 220 m s^{-1} with respect to the ground. The two radiometers pertinent to this study are the Airborne Multichannel Microwave Radiometer (AMMR) and the Advanced Microwave Moisture Sounder (AMMS) (Kramer 1994). Our purpose in this paper is to retrieve the precipitation characteristics from radiometric data, but the available Airborne Rain Mapping Radar (ARMAR) (Durden et al. 1994) profiles have been very helpful in validating the retrievals. The three instruments previously mentioned present an optimal configuration for our purpose, as they were located on the same platform, allowing us to see at the same time and from the same point of view (nadir) the different atmospheric features. Since the structures of the observed system are easier to identify from the radar observations, we present the radar data before the radiometric data.

a. Radar data

The ARMAR radar has been developed by NASA/Jet Propulsion Laboratory for the purpose of supporting future spaceborne rain radar systems, including the Precipitation Radar (PR) for the TRMM. ARMAR operates with the PR frequency and geometry, measuring reflectivity at 13.8 GHz, in a cross-track scan $\pm 20°$ from nadir along the flight track of the aircraft. ARMAR also measures the brightness temperature at 13.8 GHz between two radar measurements. In this study we selected the nadir (incidence angle $0° \pm 2°$) value of each scan both in active and passive mode. The ARMAR-measured T_B at 13.8 GHz is only used for comparison and not taken into account in the inversion scheme. This comparison is done in order to check the quality of the inversion method and is presented in detail in section 5.

The obtained reflectivity vertical cross sections are presented in Fig. 3. Note that reflectivity values below 500-m altitude should not be considered because they are contaminated by surface echo. A quick look at these profiles allows us to distinguish the three different kinds of precipitation structures that we choose to classify as follows. First, precipitating regions with evidence of a bright band are called ''stratiform.'' These regions are vertically stratified and extend horizontally because the vertical velocities are weak (less than 1 m s^{-1}), which leads to the presence of a well-defined melting layer from the 273-K isotherm to 700 m below. Such situations may be observed in the major part of leg 3 (F, Fig. 3c) and at the end of leg 5 (K, Fig. 3e). Second, regions without a bright band and having high reflectivity (greater than 30 dBZ) with a small horizontal scale and greater vertical extent are called ''convective.'' In these regions there are significant vertical velocities that ensure an important vertical mixing of the different phases of water, with an important production of precipitation that leads to high reflectivity values and to high rainfall rates. Such structures can be seen at the beginning and end of the first and second legs (Z, A, B, C, D, E, G, Fig. 3) or in the middle part of the last one (J, Fig. 3). Note that the region of leg 1 marked with a ''Z'' is unfortunately not in the domain of observation of the tail radars. Finally, the last type of region is called ''clear air'' and represents portions of the legs not classified as either convective or stratiform. One has to be aware that these clear-air zones may be cloudy or weakly precipitating (less than 2–4 mm h^{-1}). Regions I in leg 5, H in leg 4, or the portion of leg 2 between C and D are considered as clear air. In the following comments and figures, these letters will be used to locate a given region in the legs. Table 1 summarizes the characteristics of the different noted regions for each leg. These identified regions have also been plotted in Figs. 2a,b to show the horizontal geometry of the five legs. It has to be noted that the aircraft flew over the regions noted A, B, and C twice.

The ARMAR radar dataset may be considered as an independent measure of the value of the liquid rain rate (LRR) along the DC8 trajectory. These LRRs, which are used to compare with radiometric retrievals, are obtained from the radar reflectivity using the ''KZS'' algorithm described in Marzoug and Amayenc (1994). This algorithm calculates an LRR vertical profile corrected for reflectivity attenuation effects. The KZS algorithm requires as input relationships among the re-

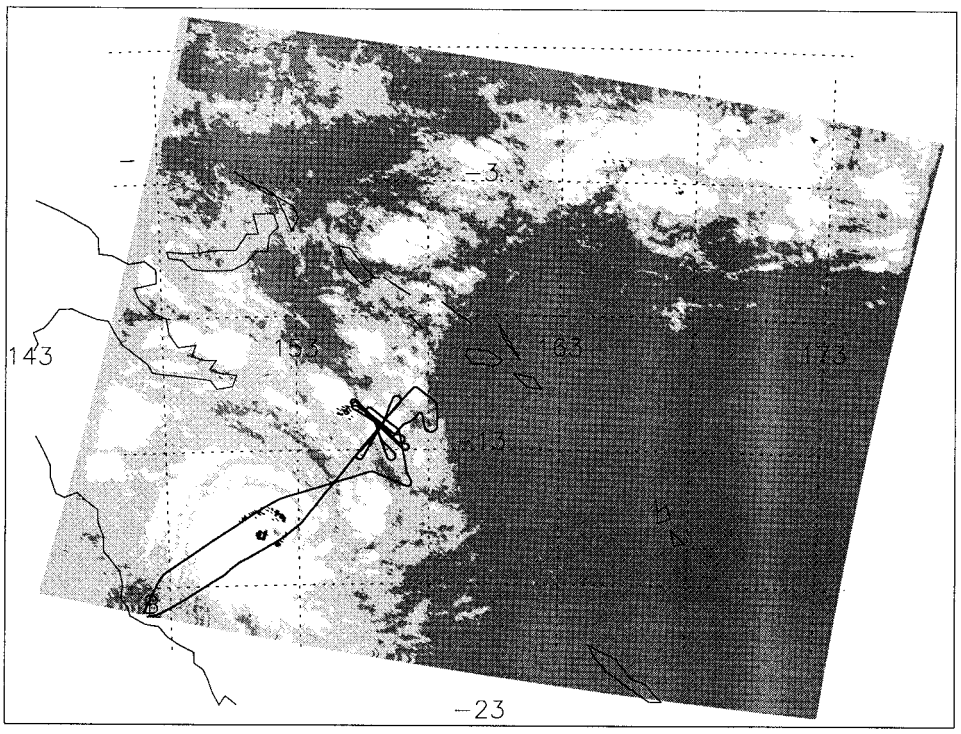

FIG. 1. OLS infrared image over TOGA COARE region, 1832 UTC 6 February 1993. The solid line indicates the NASA DC8 trajectory from 1435 to 2137 UTC. In the region where data are available, dark gray stands for 310–270 K, light gray stands for 270–230 K, and white stands for 230–190 K.

flectivity, attenuation, and the rainfall rate. The relationships used in the present study are derived from the microphysical data collected in the 6 February system by the NCAR Electra (Marécal et al. 1997). Since these microphysical relationships are more representative of convective than of stratiform precipitation, the KZS rainfall rate is more reliable for the former and tends to slightly overestimate the latter. From the vertical profiles of radar rainfall rate, a retrieved-equivalent LRR has been computed. First, a vertical average from 500-m to 4-km altitude (just below the bottom of the melting layer) ensures that the radar LRR represents the same integrated signal as for brightness temperature. Second, a horizontal filter (Cressman 1959) eliminates all the variations at a smaller scale than the resolution of the radiometric data. The obtained alongtrack profiles are presented and discussed in section 5b(2).

b. Radiometric data

The AMMR includes AMMR-1 and AMMR-2. AMMR-1 consists of a single-beam, microwave radiometer operating at 18.7, 21, and 37 GHz, all viewing through the nadir port of the aircraft. AMMR-2 is a single-beam microwave radiometer that is useless in our study for geometric reasons (view angle at 45° on the left side of the aircraft).

The AMMS is a four-channel, mechanically scanned, imaging microwave radiometer operating at 92, 183.3 ± 2, 183.3 ± 5, and 183.3 ± 9 GHz. During TOGA COARE, the beam was scanned in 25 steps of 1.8° from nadir to the left of the aircraft track. In this study, only AMMS data collected at nadir by the 92-GHz channel are utilized because higher frequencies will not be present aboard the TRMM platform.

The brightness temperature sets we selected in this study for the different legs come from the three frequencies of AMMR-1 and the 92-GHz channel of AMMS. They will be referred to hereafter as T_{B19}, T_{B21}, T_{B37}, and T_{B92}, respectively. The collocation of the data is done using only the time coincidence of each measure on both instruments. Since the AMMS sampling frequency at nadir is lower than the AMMR, this requires a resampling every 4 s of the radiometric data (and filtered ARMAR data).

The brightness temperature datasets are presented in Fig. 4. Examination of these datasets reveals that the different brightness temperatures are directly correlated with the atmospheric structure when compared to the ARMAR vertical profiles of reflectivity (see Fig. 3). The different types of regions defined above may be analyzed from their brightness temperature signature at the different frequencies. As a very general rule, it may be seen that the clear-air regions are usually characterized by low T_{B19} (mean at about 188 K), T_{B21} (mean at about 218 K), and T_{B37} (mean at about 220 K). In such a case,

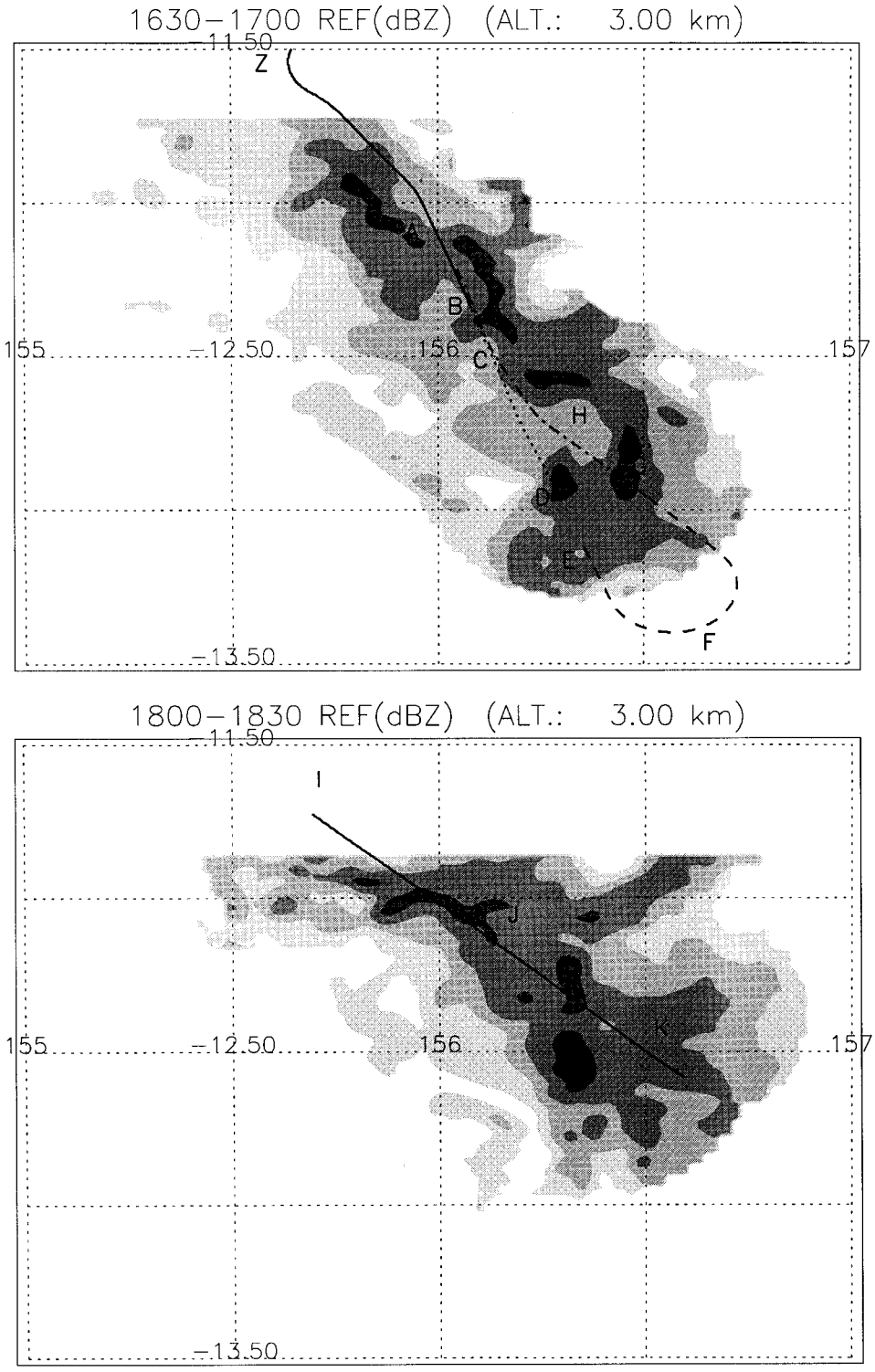

FIG. 2. Reflectivity field at 3-km altitude deduced from the combination of NCAR Electra and NOAA P3's tail radar measurements. Each composite is half-hour data for, respectively, (a) 1630–1700 UTC and (b) 1800–1830 UTC. Increasing shades of gray stand for 9, 18, 27, and 36 dBZ. The different legs of the DC8 have been plotted for each of the two composites: (a) leg 1 (solid), leg 2 (dotted), leg 3 (dashed), leg 4 (dash-dotted), and (b) leg 5 (solid). Letters refer to regions of interest (see section 3a for explanation).

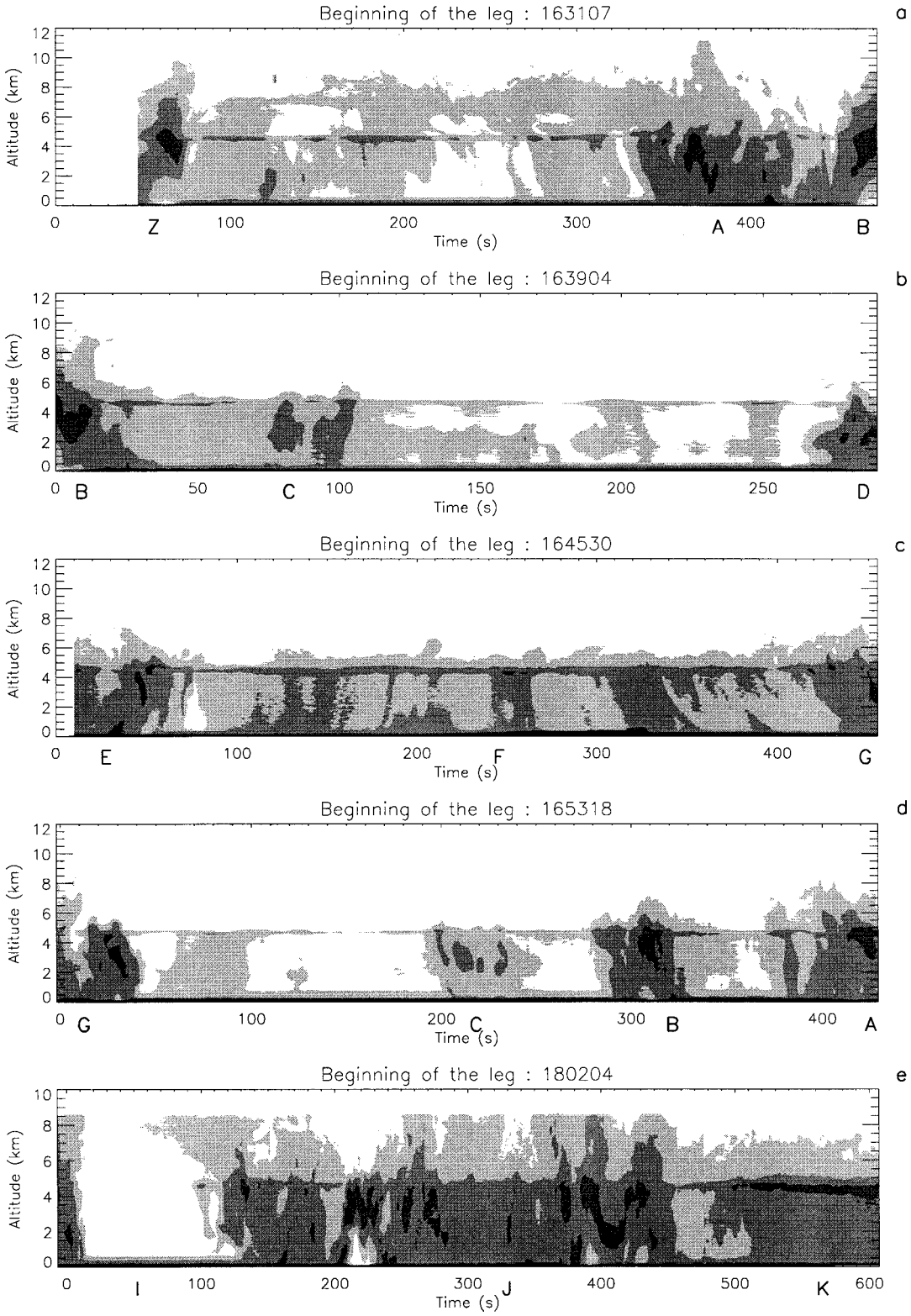

FIG. 3. Vertical cross sections of radar (ARMAR) reflectivity. Increasing shades of gray stand for 20, 30, 40, and 50 dBZ, respectively. Panels (a)–(e) refer to legs 1–5, respectively.

TABLE 1. Characteristics of the different interesting regions selected in each of the five legs. Notice that the same region (same letter) may be observed from a different point of view during two different legs.

Mark	Leg number	Start time(s)	End time(s)	Type
Z	1	35	80	Convection
A	1	330	410	Convection
B	1, 2	440 (leg 1)	30 (leg 2)	Convection
C	2	60	110	Convection
D	2	250	285	Convection
E	3	20	70	Convection
F	3	80	410	Stratiform
G	3, 4	420 (leg 3)	40 (leg 4)	Convection
H	4	100	200	Clear air
C	4	190	240	Convection
B	4	280	330	Convection
A	4	370	420	Convection
I	5	20	110	Clear air
J	5	130	450	Convection
K	5	480	600	Stratiform

T_{B92} is high, with a mean value at about 269 K. The convective regions present a higher T_{B19} (mean at about 249 K), T_{B21} (mean at about 263 K), and T_{B37} (mean at about 247 K). This increase of the mean value is mainly due to emission by liquid precipitation that is produced in the updrafts. The presence of ice particles leads to a minimum T_{B92} (mean at about 233 K) because of scattering. The stratiform precipitation presents another configuration of intermediate T_{B19}, T_{B21}, and T_{B37} (means of about 205, 233, and 231 K, respectively). These intermediate values are due to the expected lower rainfall rates when compared with the convective cases that induce a weaker emission from raindrops. The T_{B92} in stratiform situations is also intermediate with a mean value at about 254 K, indicating a weaker ice scattering.

4. The RTM and its inversion

a. The microwave RTM

The original radiative transfer model (RTM) used for the calculation of microwave upwelling brightness temperature was described by Kummerow and Weinman (1988). It is not our purpose to review in detail the principles of this RTM, but its main characteristics are recalled here. It is based on the Eddington approximation for a multilayered plane-parallel medium. Brightness temperatures are expanded in a series of Legendre and associated Legendre functions. The phase function is similarly expanded in Legendre polynomials. The albedo for single scattering is readily obtained from the Mie theory, assuming spherical particles. The solution referred to as the ''finite difference Eddington solution'' is detailed in Wu and Weinman (1984). This type of model is easy to operate and fast, but it is unable to take correctly into account the vertical distribution of hydrometeors. Nevertheless, Kummerow et al. (1996) have shown, comparing it with a Monte Carlo scheme model, that the mean difference at 85 GHz (19 GHz) is about 2.7 K (1.2 K) and can reach 12 K (5.3 K) in very strong precipitation. These differences are of the same order as those we obtain when fitting the T_B's into the inversion procedure.

This RTM takes into account surface emission, cosmic background radiation, atmospheric absorption by water vapor, atmospheric absorption by molecular oxygen, absorption by cloud liquid water, and both absorption and scattering by liquid drops and ice particles. Then, the different parameters used by the RTM to calculate the emerging brightness temperatures are of two types. First, the surface is assumed to be specular and it is necessary to know its characteristics: the sea surface skin temperature and the surface wind speed for the surface emissivity calculation. Second, the RTM needs the characteristics for each layer: altitude and temperature at the layer top, average relative humidity, average cloud liquid water content (CLW), average liquid rainfall rate (LRR), and average ice rainfall rate (IRR).

b. The inversion

As previously explained, the RTM computes an emerging T_B from a simplified atmospheric model. To ''invert'' the RTM means that we iteratively look for the set of atmospheric characteristics that leads the RTM to calculate simulated T_B's as closely as possible to the observed T_B's. This inversion is made numerically. A set of initial values for the unknowns is necessary; we will discuss below the choice of these initial values and their influence on the solution. The inversion is done iteratively from the initial values, calculating at each iteration the following estimate:

$$\chi^2 = \sum_{i=1}^{N_{TB}} \mu_i (T_{B\text{simi}} - T_{B\text{mesi}})^2,$$

where N_{TB} is the number of independent frequencies used in the retrieval, which corresponds to the number of independent brightness temperatures to adjust. The $T_{B\text{simi}}$ and $T_{B\text{mesi}}$ are, respectively, the simulated and measured brightness temperatures for the ith frequency. The coefficient μ_i is a weight that allows us to control possible problems in the quality of the data at a given frequency. The determination and influence of this weighting will be discussed below.

The calculated χ^2 is used in the E04JAF-NAG Library Routine, which consists of a quasi-Newton method (Gill and Murray 1976), to calculate the new set of the unknown values. This new set of physical variables is then used to compute a new set of simulated brightness temperatures and a new iteration is initiated. This iterative method stops when the latest calculated χ^2 is a minimum in a mathematical sense. This method gives no information about the physical sense of the results because some local minima may be found that are not representative of the actual atmospheric situation. Another

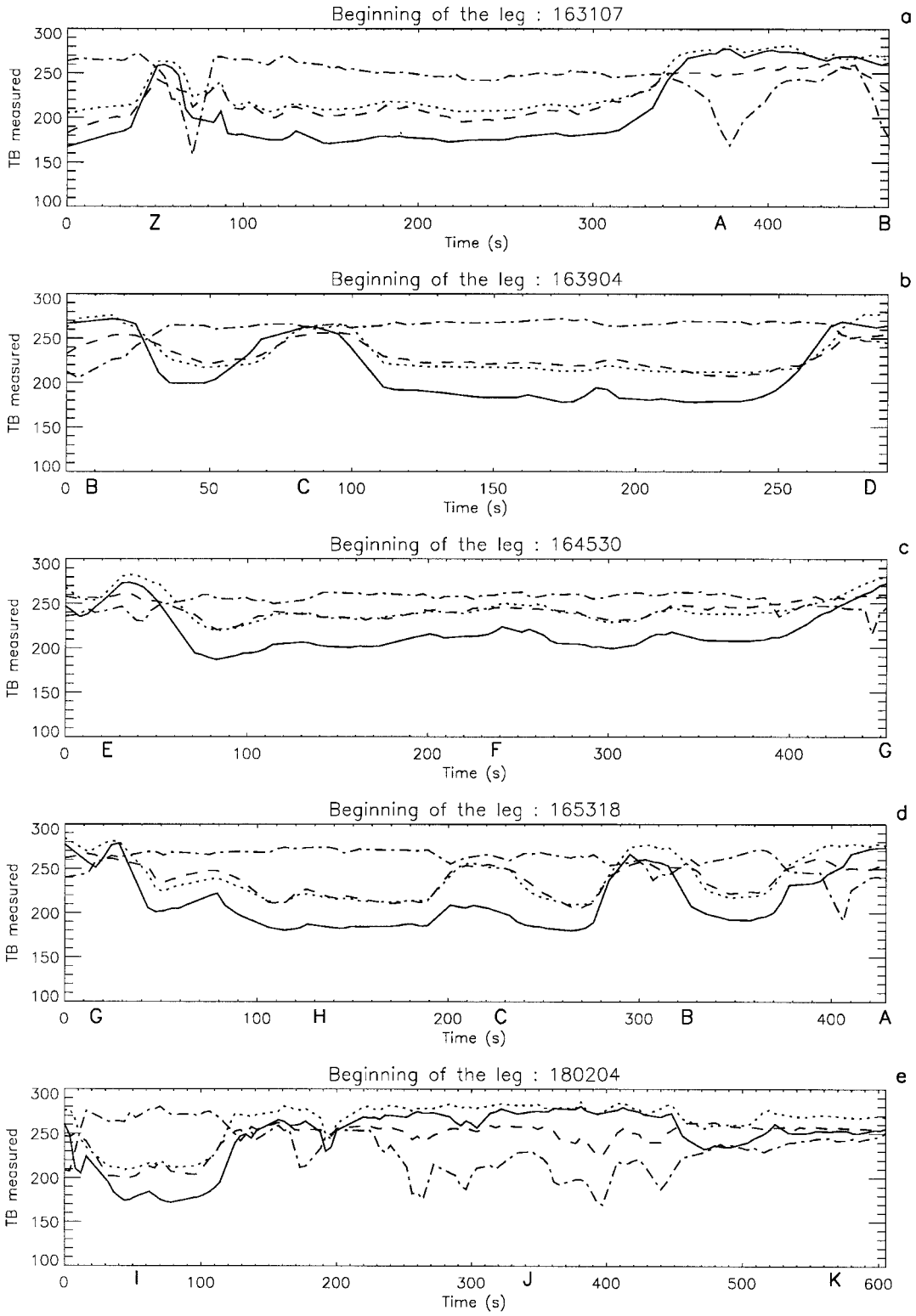

FIG. 4. AMMR- and AMMS-measured brightness temperature (K) at 18.7 (solid line), 21 (dotted line), 37 (dashed line), and 92 GHz (dash-dotted line). Panels (a)–(e) refer to legs 1–5, respectively.

mathematical constraint is the necessary independence of the different variables to retrieve, which is verified in the present case.

The procedure of inversion must be overdetermined due to the noise in the measurements and the possible ambiguity of the solution. So the four utilized brightness temperatures allow us to retrieve only three physical variables. We have considered that in the precipitating regions the most important phenomena are scattering and absorption by both ice particles and liquid drops. In such cases, the influence of cloud particles is weak, but wherever precipitation rates are low, the cloud particles signal dominates. This is why the rainfall rates for liquid (LRR, mm h^{-1}) and ice (IRR, mm h^{-1}) and the cloud liquid water content (CLW, g m^{-3}) have been chosen to be retrieved. Recall that the ice cloud is not taken into account in the RTM because of its negligible influence in most cases.

As we only have three unknowns, the atmosphere is represented as two plane-parallel layers. The transition level from ice to liquid is the 273-K isotherm. The first layer extends from the ground to the 273-K isotherm, and the second one extends from the 273-K isotherm to the aircraft flight altitude. LRR and CLW are both vertically averaged values in the first layer, while IRR is vertically averaged in the second one. Note that the melting layer, when it exists, is included in the liquid water layer. This choice has been made because it induces the smallest error on calculated T_B. In convective regions there is no ''bright band effect.'' On the other hand, in stratiform regions, values of the backscattering coefficients of melting particles are closer to those of liquid water than those of ice particles. This effect, more important for low microwave frequencies, has been described by Obligis and Klapisz (1996).

The problem in convective regions is the effect of mixing by up- and downdrafts. In such cases, the vertical velocities may be strong enough to induce formation and/or transportation of raindrops above the freezing level and transportation of ice particles below. This effect is not taken into account in our two-layer atmospheric model. Nevertheless, Takahashi et al. (1995) present videosonde observations in which the amount of liquid water above the 0°C isotherm is weak in a rainband associated with a typhoon (in the COARE region in November 1991). Moreover, LeMone and Zipser (1980), Zipser and LeMone (1980), and Jorgensen and LeMone (1989) also present results showing that updrafts are generally weak in oceanic tropical convective systems. This indicates that small amounts of liquid particles are expected above the freezing level in TOGA COARE convective cells. This supports the choice of the 0°C isotherm level as intermediate boundary between the two layers in the RTM.

c. Input data

As previously mentioned, it is necessary to constrain some of the input atmospheric parameters for the RTM to allow the computation of the merging T_B's. First, the temperature profile is determined using the data from vertically falling sondes dropped by the DC8. The temperature ranges from 302 K at sea surface to 242 K at 10-km altitude. The 273-K isotherm level is at 4.7-km altitude. Second, the relative humidity is set to 97%, which represents a consistent value in precipitating regions. Third, the mean value for surface wind is chosen at 2.0 m s^{-1}, which corresponds to a calm atmosphere with neither convective nor stratiform precipitation. This value is coherent with the results presented in Ali-Mehenni and Testud (1995), using Doppler radar data in the vicinity of TOGA COARE convective systems. Sensitivity tests showed that the influence of surface wind variation from 1 to 15 m s^{-1} is rather weak: less than 10 K (for T_{B19} and for null CLW, LRR, and IRR). Fourth, the mean SST is chosen equal to 302 K, which corresponds to the mean monthly value in this region. Another sensitivity test showed that the influence of SST on T_{B19} is also weak: less than 8 K for a sea surface temperature ranging from 290 to 310 K (for null CLW, LRR, and IRR). At 37 GHz, this influence is lower than 3 K for the same variation of SST.

The values of these four last constants vary from precipitating to nonprecipitating regions and may even vary with respect to the rain rate. Nevertheless, they may be considered as secondary because their influence on the emerging T_B's computation is much weaker than the contribution of LRR, IRR, and CLW in both convective and stratiform regions. In nonprecipitating but cloudy zones, the CLW remains the dominant factor.

In the RTM, the rain and ice distributions are assumed to follow an exponential shape of the form $N(D) = N_0 \exp(-\lambda D)$, where D is the diameter of the particles. Each of the N_0 coefficients for rain and snow is assumed to be constant. For rain, we used the $N_0 = 4 \times 10^7$ m^{-4} value that was derived from the analysis of the microphysical data collected on board the Electra (NCAR). This new raindrop distribution included in the RTM is substituted for the original Marshall–Palmer distribution (Marshall and Palmer 1948). To determine the LRR from the rain size distribution, the fallspeed–diameter relation proposed by Atlas and Ulbrich (1977) was used.

An ice precipitation density representative of the whole ice layer (between 4.7- and 10-km altitude) has to be set in the RTM. We looked for a value that was acceptable for both convective and stratiform precipitation. Information about ice-phase microphysics in TOGA COARE is localized in space (McFarquhar and Heymsfield 1996; Takahashi et al. 1995). Although this information is valuable, it does not provide the global estimation we need about a mean value for ice density. We choose a density of 0.2 g cm^{-3}, which is an average between the stratiform (0.1 g cm^{-3}) and the convective (0.3 g cm^{-3}) regions. To support our choice, results from Global Atmospheric Research Program (GARP) Atlantic Tropical Experiment (GATE) and Taiwan Area Mesoscale Experiment (TAMEX) indicate weak convective

TABLE 2. Statistical results for T_B's fits. Here ΔT_B stands for $T_{B\text{retrieved}} - T_{B\text{measured}}$. and $\sigma\Delta T_B$ stands for standard deviation of the above-mentioned difference.

Total number of points: 395	Clear air (68 points)	Convective (177 points)	Stratiform (150 points)
Mean ΔT_{B19}	−8.03	−0.39	−7.25
Mean ΔT_{B21}	2.40	−1.62	−0.27
Mean ΔT_{B37}	3.70	7.68	8.62
Mean ΔT_{B92}	−0.49	−1.11	−1.08
$\sigma\ \Delta T_{B19}$	5.15	5.01	6.40
$\sigma\ \Delta T_{B21}$	2.32	6.18	4.50
$\sigma\ \Delta T_{B37}$	3.89	6.05	6.79
$\sigma\ \Delta T_{B92}$	1.00	6.82	0.92

updrafts over tropical oceans (LeMone and Zipser 1980; Zipser and LeMone 1980; Jorgensen and LeMone 1989). These weak upward motions do not allow heavy riming and probably lead to low to moderate graupel density for ice in convection. This problem with the ice description is tempered by the strong correlation between ice phase and T_{B92} and the relative independence of this pair with respect to the three lower frequencies. Sensitivity to ice density is discussed in section 5.

5. Retrieval of atmospheric variables from airborne data

a. Quality of inversion

1) BRIGHTNESS TEMPERATURES FIT

As there is no information about error bias at any frequency, we have chosen in this study to fix the weighting μ_i (i = [19, 21, 37, 92]) equal to 1. The initial values for LRR, IRR, and CLW are respectively chosen at 15 mm h^{-1}, 8 mm h^{-1}, and 0.2 g m^{-3}. When a convergence problem is detected by the inversion routine after 400 iterations (local minimum) the process is restarted from a different set of initial values twice greater or lower than the above-mentioned values. Numerous tests about the inversion procedure tend to demonstrate the stability of the method: when a solution is found, it is correct both in a mathematical and in a physical sense and does not depend on the initial set of values. The double iteration process affects less than 15% of the retrieved values and does not appear as problematic from a computing-time point of view.

Accuracy of the RTM-calculated T_B is estimated at about 2–3 K, depending on the atmospheric situation (Kummerow 1993), and accuracy of the different channels of the radiometers is estimated at about 3–4 K. Thus, the total uncertainty is about 5–7 K. The differences between retrieved and measured T_B's (ΔT_B) are presented in Table 2. For the present study, the fit leads to mean ΔT_B's lower than 8 K, but its sign depends upon the frequency and the observed situation (e.g., stratiform, convective, or clear air). It may be considered roughly that the clear-air situation represents an estimation of the error of instrument calibration, of atmospheric characteristics (altitude and temperature of the layers and relative humidity), and of surface representation because in such a case there is theoretically no interaction with water particles. This consideration can help to interpret the results but did not lead to any possible systematic correction because, in this study, the clear-air situations are not precisely identifiable and thus can be cloudy or slightly precipitating.

The T_{B19} is always underestimated with a standard deviation (noted as $\sigma\Delta T_{B19}$) lower than ΔT_{B19}. It varies with the meteorological situation: a greater bias for clear-air and stratiform situations and a smaller bias for convective situations. The $\sigma\Delta T_{B19}$ does not vary more than 1 K for these different situations. These results may indicate a calibration problem for the radiometer and/or surface inhomogeneity as the ΔT_{B19} is important when the precipitation is weak (rain rate $<$ 7–8 mm h^{-1}). This is consistent with sensitivity tests of the retrieval method, showing that this frequency is more correlated with the liquid precipitation and surface characteristics than with cloud or precipitating ice.

The bias for T_{B21} is generally smaller than for T_{B19}. It is slightly positive in clear air and increasingly negative as the precipitation rate increases (i.e., from stratiform to convective situations). The standard deviation seems also directly correlated to the precipitation rate as it increases from clear air to convective situations. This loss in quality is consistent with sensitivity tests that have shown 1) a correlation between this frequency and the cloud presence and 2) where the rain rates are greater than approximately 12 mm h^{-1}, the cloud signal is masked. Nevertheless, this bias of ΔT_{B21} is smaller than the theoretical accuracy of the retrieval method.

The T_{B37} is always overestimated with $\sigma\Delta T_{B37} < \Delta T_{B37}$. In clear-air situations, the ΔT_{B37} is low with a low standard deviation. In precipitating situations, the ΔT_{B37} and $\sigma\Delta T_{B37}$ increase strongly. At this frequency T_B is certainly the most difficult to adjust because it is influenced by CLW, LRR, and IRR, and so it is highly sensitive to simulation errors. In convective situations, the mixing of the liquid and ice particles both below and above the 273-K isotherm may lead to a systematic error. In stratiform situations, the melting layer crudely taken into account may be the source of the above-mentioned error.

Finally, it has to be noted that the T_{B92} is the T_B that corresponds to the best fit, whatever the considered situation. This result is probably due to the fact that this frequency is essentially sensitive to the ice precipitation and is therefore easier to adjust. Also note that $\sigma\Delta T_{B92}$ is relatively high in the convective situation when compared to the two other categories. This may be due to the difficulty in representing the ice phase in such situations where mixing of liquid water and ice can be found above the 273-K isotherm.

2) 13.8-GHz BRIGHTNESS TEMPERATURE COMPARISON

ARMAR is able to measure the brightness temperature at 13.8 GHz (hereafter $T_{B13.8\text{mes}}$) between two radar looks. These data were horizontally filtered (Cressman 1959) to ensure the same sampling frequency as for the radiometric data. To make a direct comparison with this independent measure at 13.8 GHz, we have calculated a $T_{B13.8}$ (hereafter $T_{B13.8\text{ret}}$) from the RTM, using as an input the set of atmospheric variables retrieved. This comparison gives an indication of both the quality of the T_B's fit and of the retrieved atmospheric variables, but it is impossible to distinguish the importance of their respective contribution to error. It has to be noted that the brightness temperatures at 13.8 and 19 GHz have relatively close behavior and so a good fit of T_{B19} often leads to $T_{B13.8\text{ret}}$ close to $T_{B13.8\text{mes}}$. In precipitating regions where LRR $>$ 15 mm h^{-1}, the T_{B19} becomes affected by saturation phenomena and its behavior differs from that of $T_{B13.8}$. Thus, the comparison between $T_{B13.8\text{ret}}$ and $T_{B13.8\text{mes}}$ is more significant in convective regions.

The $T_{B13.8}$'s are presented in Fig. 5. The qualitative agreement is good, and nearly all the structures are reproduced by the retrieved $T_{B13.8}$. Important differences between the two $T_{B13.8}$'s (e.g., Z or D, Figs. 5a,b) are locally found. These regions that are associated with very specific precipitation structures are examined in detail later. The mean difference $T_{B13.8\text{ret}} - T_{B13.8\text{mes}}$ (denoted $\Delta T_{B13.8}$) depends on the considered situation: -0.76 K for clear air, -6.39 K for convection, and -6.99 K for stratiform regions. This bias is always negative, indicating a weak underestimate of the retrieved $T_{B13.8}$, which remains about the order of magnitude of the methodological error. The standard deviation of $\Delta T_{B13.8}$ (denoted $\sigma\Delta T_{B13.8}$) is about 6 K for clear air and 7 K for stratiform situations, and it increases to 28.5 K in convective situations. This last result is due to both unrealistic retrievals for the four points of the convective regions and the sensitivity of this channel to high rainfall rates for which uncertainties in the retrieved LRR are amplified in computed $T_{B13.8\text{ret}}$.

Nevertheless, the global agreement of the measured and retrieved brightness temperatures allows us to consider that both the inversion procedure and the retrieved parameters are consistent with the 13.8-GHz observations.

b. Results

1) RETRIEVED VARIABLES

Retrieved CLW, LRR, and IRR are shown in Fig. 6 for each leg, respectively. In precipitating regions, the curves representing the LRR and IRR are generally smoother than the CLW curve. This is due to the domination of the precipitation signal on the cloud that leads to the poor quality of retrieved CLW in such cases. This is why it is not possible to analyze the CLW in precipitating regions. Nevertheless, in the clear-air regions, qualitative comments can be presented, although there is no quantitative way to compare with or validate the cloud liquid water content.

Clear-air regions (e.g., H and I) are characterized by a CLW between 0 and 0.4 g m^{-3}, which is consistent with the expected values for cloudy or weakly precipitating regions. Most of these regions show no evidence of liquid precipitation or light ice precipitation (IRR $<$ 3 mm h^{-1}). These last features are generally related to the weak reflectivity signal aloft that can be observed in ARMAR data cross sections (see Fig. 3).

The retrieved IRR indicates ice presence in most of the precipitating regions, as expected. The maximum IRR are close to 30 mm h^{-1} and are obtained in the intense convective regions (Z, A, B, and J; Figs. 6a,e). It is impossible to validate the retrieved IRR in precipitating regions. The realistic maximum for LRR is up to 45 mm h^{-1} and is attained during leg 2 (B, Fig. 6b) and leg 5 (J, Fig. 6e). The maximum LRR (and null IRR) at end of legs 1 and 2 (B, D, Figs. 6a,b) appear to be artifacts from numerical inversion because for D (Fig. 3b) there is no corresponding reflectivity signal in the ARMAR data and for B (Fig. 3a) the RTM simulated $T_{B13.8\text{ret}}$ is unrealistic.

A survey of retrievals in the convective regions yields two different regimes. The first one shows both liquid and ice precipitation. Such cases are found at the end of leg 1 (A, Fig. 6a), at the beginning of leg 2 (B, Fig. 6b), and in the middle part of leg 5 (J, Fig. 6e). In all of these regions, a clear signature of both ice and liquid precipitation presence is given in the ARMAR reflectivity picture (Figs. 3a, 3b, and 3e, respectively). This configuration may be considered as the classic structure of tropical convection, where precipitation is present in both liquid and ice phases. Complementary information about vertical velocities deduced from Doppler radar show that these regions correspond to sustained updrafts.

The second case presents weak ice phase precipitation as compared to the liquid phase. Examples of such a feature is given by the region C, visible in legs 2 and 4 (Figs. 6b,d). This is the border of a convective cell. Doppler data show that this cell is driven by east and west winds, converging at low levels (altitude lower than 5 km). In this case, the west wind is stronger, inducing the cell to be lightly tilted toward the east. So, the ice-phase precipitation develops only to the east of the aircraft and so is not visible at nadir.

In region Z (Fig. 6a), only liquid water is present at first, which leads to maximum values for the T_Bs at low and medium frequencies (absorption by raindrops). Farther along the flight track, ice presence induces a T_{B92} drop. The interpretation is that the air is upraised at the front of the cell, inducing liquid precipitation first, and then the following upward air motion induces both liquid and ice precipitation in the rear side. This hypothesis is supported by the ARMAR reflectivity profile (Fig.

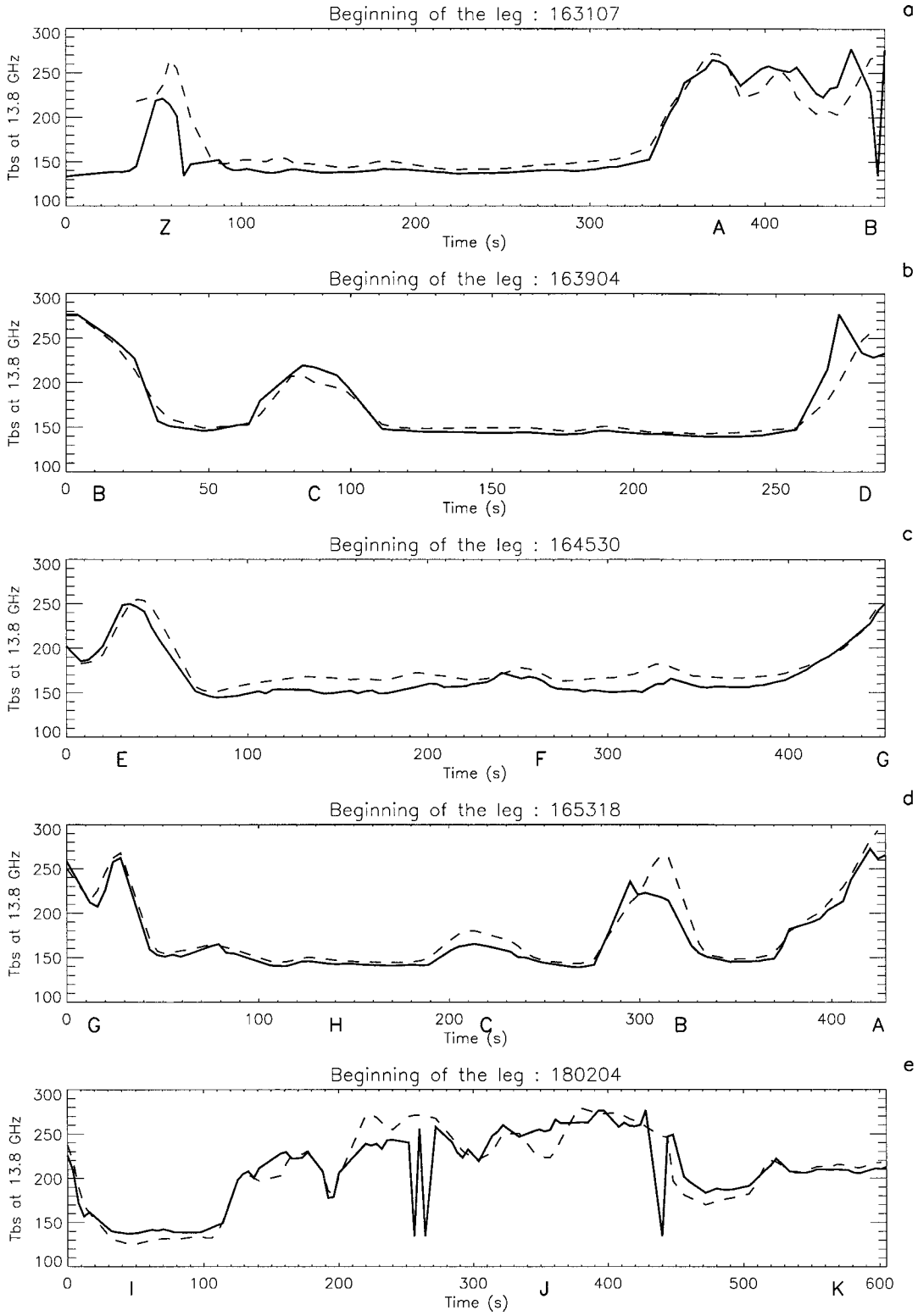

FIG. 5. ARMAR-measured 13.8-GHz brightness temperature (*K*, dashed line) and RTM-simulated 13.8-GHz brightness temperature (*K*, solid line).

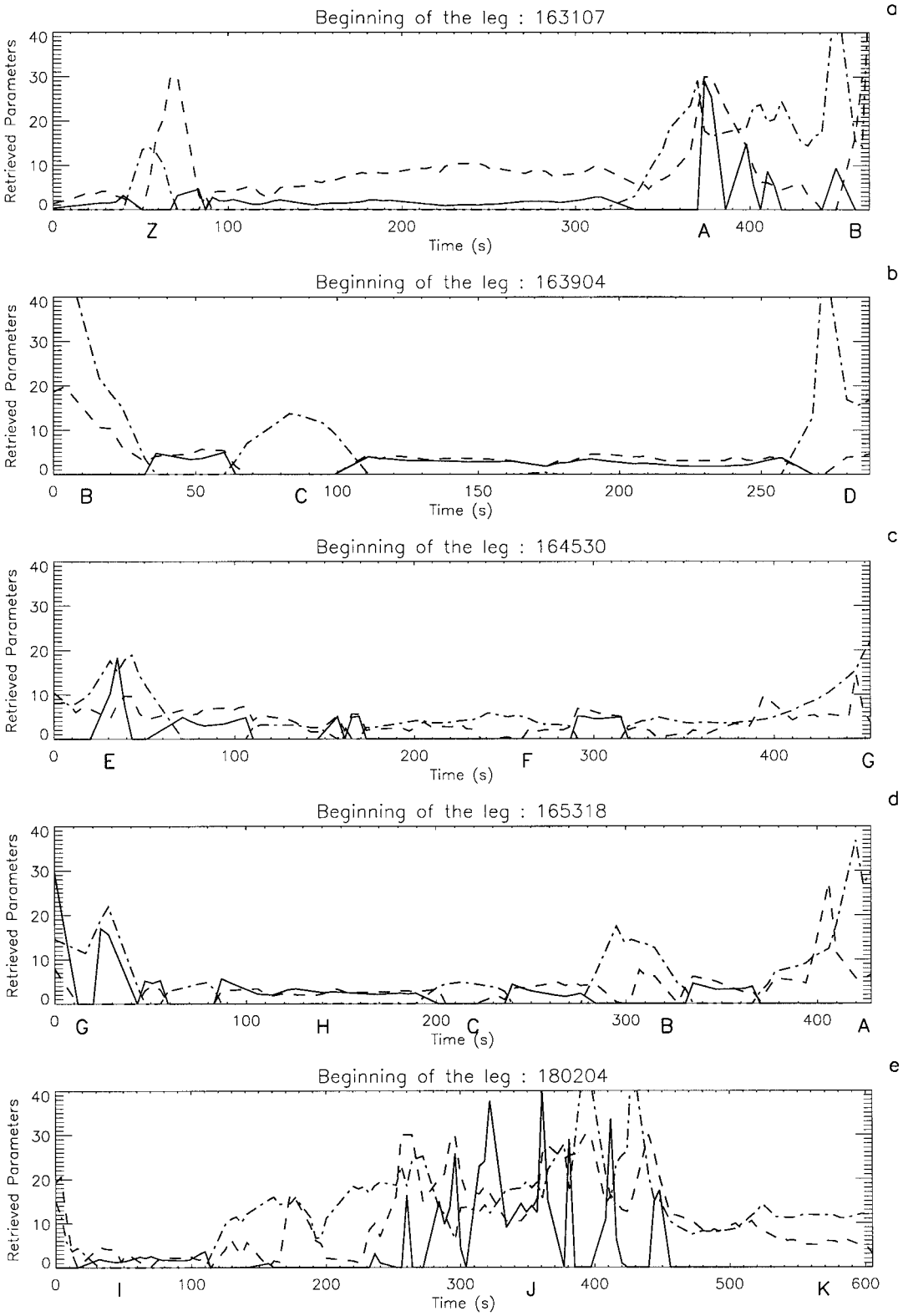

FIG. 6. Retrieved parameters: IRR (mm h^{-1}) in the upper layer (dashed line), CLW (10^{-1} g m^{-3}) in the lower layer (solid line), and LRR (mm h^{-1}) in the lower layer (dash-dotted line). Panels (a)–(e) refer to legs 1–5, respectively.

3a), where evidence of such a structure can be observed. This interpretation is consistent with the retrieved LRR and IRR except that LRR decreases as soon as IRR $>$ 15 mm h^{-1} (t = 50 s). These low LRR values are probably underestimated since the use of direct RTM shows that the $T_{B13.8\text{mes}}$ in region Z (about 265 K) corresponds to high liquid rain rates (30–40 mm h^{-1}). The underestimation of the retrieved LRR can be related to the inversion procedure that provides a bad fit of the T_B's in this region: large underestimaton of the T_B's at 92 and 18 GHz and large overestimation of T_B's at 37 and 22 GHz. This fitting problem may be related to the large mixing of ice/liquid particles that probably occurs above and below the 0°C isotherm. This mixing cannot be taken into account in the retrieval procedure where a two-layer atmosphere is assumed (only liquid particles below the 0°C isotherm and only ice particles above).

Finally, the last type of observed results is for stratiform regions such as F and K (Figs. 6c,e, respectively). IRR and LRR retrieved for K are greater than those retrieved for F. This is consistent with the ARMAR reflectivity profile (see Figs. 3c,e) that shows that F is less than K with a lighter brightband effect.

Influence of ice density has been tested through different retrievals. On the one hand, the retrieved IRR tends to decrease as the ice density increases; on the other hand, the LRR is nearly not modified by ice density value. When ice density passes from 0.2 to 0.5 g m^{-3}, the LRR is not modified by more than 4%. This may be explained by the weak ice-scattering effect on T_{B37} over tropical oceans because of the weak observed updrafts (McGaughey et al. 1996b). In stratiform regions, the choice of a smaller (less than 0.2 g cm^{-3}) density (and so a more realistic) will lead to a higher IRR. In convective regions, the opposite effect will lead to reducing the retrieved IRR.

2) LRR COMPARISONS

In the following comments, ''radiometric LRR'' refers to LRR retrieved through the inversion of the RTM, and ''ARMAR LRR'' refers to LRR deduced from ARMAR radar data, as described in section 3a. A summary of the main statistical results of this LRR comparison is given Table 3. For clear-air, convective, and stratiform regions, the mean LRRs found by the two independent methods are close with very similar values of standard deviation. Note that σ is generally close to the mean LRR, indicating an important dispersion of the rain-rate values. The ratio indicates that the most important error is observed in a clear-air region, but in such a case, the rain rates are low, inducing a strong relative error.

Comparison between the two LRRs is presented in Fig. 7. This figure allows us to verify the agreement from a structural point of view. It has to be noted that all the maxima are located at the same place for both datasets, even if very local discrepancies may be observed. Interesting cases may be emphasized. First, in the Z region (Fig. 7a), there is an important discrepancy between the radar LRR and the radiometric LRR. The radar LRRs indicate high rain rates that are not retrieved by the radiometric approach. As discussed in the previous section, the poor quality fit provided by the inversion procedure in region Z leads to the underestimation of the radiometric LRRs. Second, in regions of very low precipitation, where ARMAR LRR $<$ 2 mm h^{-1} (e.g., Fig. 7b between regions C and D), the RTM LRR is generally found at 0 mm h^{-1}. This result indicates that such rain rates are under the sensitivity threshold of the retrieval method. This threshold is correlated with both the instrumental noise and the accuracy of the RTM (typically 2–3 K). Such an effect can also be observed in weak stratiform precipitation. Nevertheless, note the good agreement between the two LRRs in stratiform regions F and K. Third, the shape of the RTM LRR curve is smoother than the shape of the ARMAR LRR, especially in convective regions. This may be due to the larger size of radiometric pixels for which the horizontal extent has not been taken into account when compared with the radar transverse pixel size.

Finally, influence of the modified DSD may be easily quantified in this comparison with ARMAR data. With the original distribution (Marshall and Palmer 1948), the mean retrieved LRR's are 0.60 mm h^{-1} in clear-air regions, 9.69 mm h^{-1} in convective regions, and 2.61 mm h^{-1} in stratiform regions. With the new DSD, the values for precipitating regions are much closer to those of the ARMAR, and a comparison of the LRR profiles (not shown here) demonstrates a better point-to-point fit, especially in convective regions. This result points out the importance of the DSD characteristics on the retrieved rain rates.

TABLE 3. Statistical results for RTM-retrieved and ARMAR-deduced LRR following the different atmospheric situations. Here σ stands for standard deviation, bias stands for mean RTM LRR minus mean ARMAR LRR, ratio stands for the ratio between RTM LRR over ARMAR LRR, and rms error stands for the root-mean-square error.

Total number of points: 395	Clear air (68 points)	Convective (177 points)	Stratiform (150 points)
Mean radar (mm h^{-1})	0.86	14.24	3.55
Mean radiometer (mm h^{-1})	0.34	14.60	3.14
σ radar (mm h^{-1})	0.58	14.59	2.99
σ radiometer (mm h^{-1})	1.11	10.39	3.92
Bias (mm h^{-1})	−0.51	0.36	−0.41
Ratio	0.40	1.02	0.88
Mean absolute error (mm h^{-1})	0.83	7.24	1.62
rms error (mm h^{-1})	0.98	12.07	1.96

6. Conclusions

The TOGA COARE experiment and especially the 6 February 1993 case has provided a very complete observation of an MCS, drawing upon data from numerous

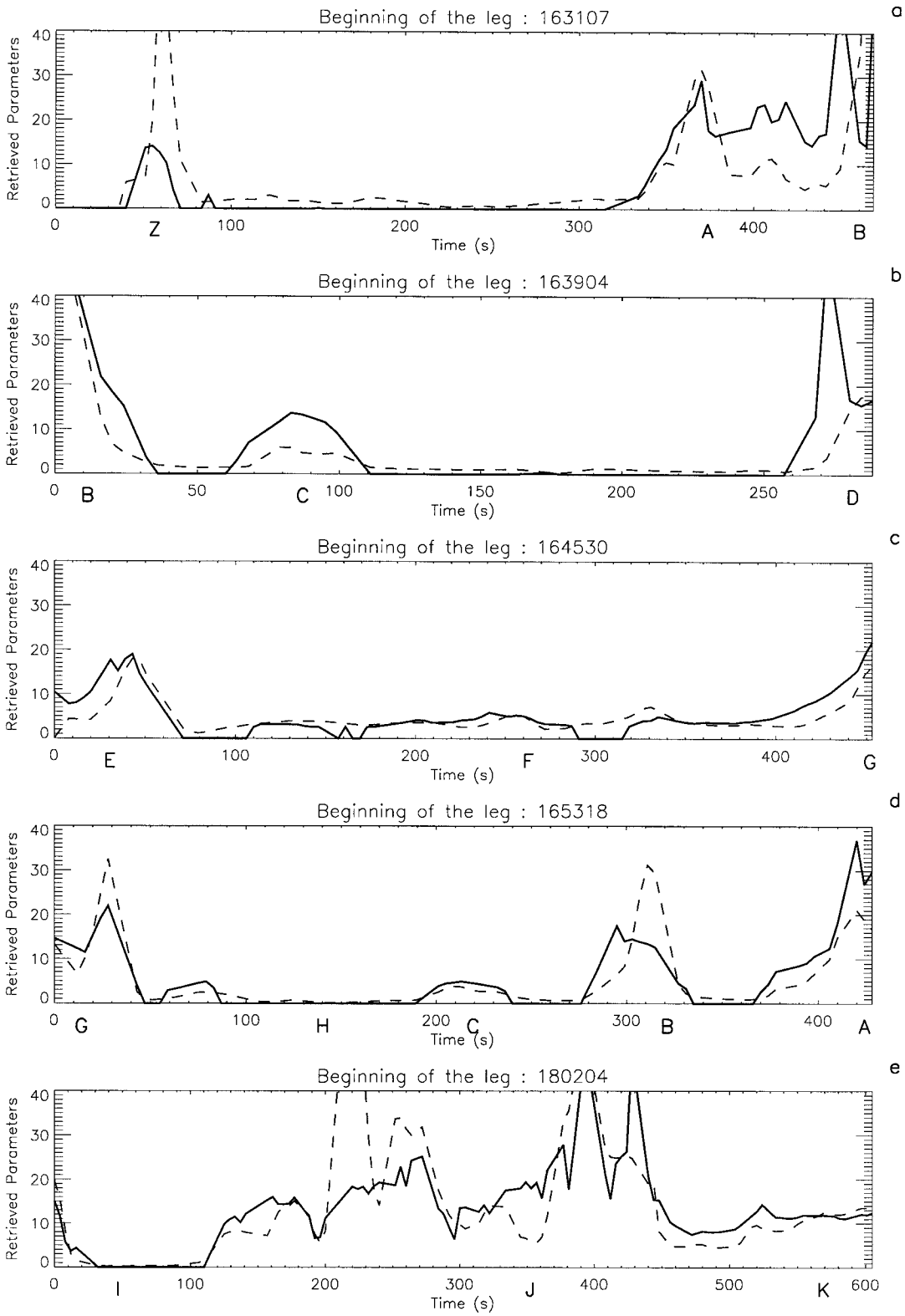

FIG. 7. ARMAR-deduced LRR (mm h^{-1}, dashed line) and RTM-retrieved LRR (mm h^{-1}, solid line). Panels (a)–(e) refer to legs 1–5, respectively.

different instruments. The purpose of this study was to numerically invert an RTM in order to retrieve ice and liquid precipitation rates and cloud liquid content from aircraft-measured T_B's at 18.7, 21, 37, and 92 GHz. The liquid rain rate and the cloud liquid water content are retrieved as a vertically averaged value over the liquid layer (0–4.7 km) and the ice rain rate is retrieved as a vertically averaged value over the ice layer (4.7–10 km). The quality of the fit of each of the T_B's was found to be consistent with respect to both RTM and instrumental accuracy (5–7 K). Comparison with independently measured T_B at 13.8 GHz also pointed out the consistency of the retrieval.

The retrieved variables have been interpreted with the help of three-dimensional reflectivity and wind fields from Doppler tail radar from three other aircraft. The conjunction of these data sources allowed us to verify the consistency of the retrieved LRR and IRR in the precipitating regions and, in a lesser way, of retrieved CLW in the other regions: order of magnitude for convective and stratiform regions, presence of ice precipitation correlated with cell structure, and presence of cloud in the lower precipitating regions.

The results have also been compared to LRR deduced from ARMAR (radar) data from the same platform. The comparison of radar- and radiometer-deduced LRR, over 400 observations, showed a good agreement, with a mean relative bias lower than 3% (overestimate) in convection and lower than 12% (underestimate) in stratiform precipitation. The use of microphysical data allowed us to prescribe a more appropriate drop size distribution in the radiative transfer model. The impact of this modification has been emphasized by the comparison to ARMAR-deduced rain rates.

By combining data from different instruments we have tried to give a better understanding of the influence of the structure of the observed system onto the measured T_B's and to improve the comprehension of the physical retrieval approach.

Acknowledgments. The authors acknowledge F. Roux (from Laboratoire d'Aérologie, Toulouse, France) for providing us with the tail radar reflectivity and wind field composites used to perform the analysis and reproduce Figs. 2a,b, and R. Bauer (from National Snow and Ice, Boulder, Colorado) for providing us with the OLS–IR data reproduced in Fig. 1. We are also indebted to T. Tani and P. Amayenc (CEPT) for providing KZS-deduced LRR and the reflectivity profiles from ARMAR. We express our appreciation to F. Marks, P. Willis, and R. Black (from NOAA/AOML, Miami, Florida) for providing the experimental Electra drop size spectra used to determine the characteristics of the rain distribution. We would like to thank the Process Studies Program Office (Code SEP, NASA Headquarters) and the Distributed Active Archive Center (Code 902.2) at Goddard Space Flight Center, Greenbelt, Maryland, for the production and distribution, respectively, of the AMMR, and AMMS and ARMAR data. The remarks made by the three anonymous reviewers greatly helped to improve the paper.

REFERENCES

Adler, R. F., H. Y. M. Yeh, N. Prasad, W. K. Tao, and J. Simpson, 1991: Microwave simulations of a tropical rainfall system with a three-dimensional cloud model. *J. Appl. Meteor.*, **30,** 924–953.

——, A. J. Negri, P. R. Keehn, and I. M. Hakkarinen, 1993: Estimation of monthly rainfall over Japan and surrounding waters from a combination of low-orbit microwave and geosynchronous IR data. *J. Appl. Meteor.*, **32,** 335–356.

Ali-Mehenni, M., and J. Testud, 1995: Sea surface winds estimation using airborne Doppler weather radar. *Int. Geoscience and Remote Sensing Symp.*, Florence, Italy, IEEE/ESA, 831–833.

Atlas, D., and C. W. Ulbrich, 1977: Path and area integrated rainfall measurements by microwave attenuation in the 1–3-cm band. *J. Appl. Meteor.*, **16,** 1322–1331.

Cressman, G. W., 1959: An operational objective analysis system. *Mon. Wea. Rev.*, **87,** 367–374.

Durden, S. L., E. Im, K. Li., W. Ricketts, A. Tannier, and W. Wilson, 1994: ARMAR: An airborne rain-mapping radar. *J. Atmos. Oceanic Technol.*, **11,** 727–737.

Gill, P. E., and W. Murray, 1976: Minimization subject to bounds on the variables. National Physical Lab. Rep. NAC 72. [Available from National Physical Laboratory, Teddington, Middlesex TW11 0LW, United Kingdom.]

Grody, N. C., 1991: Classification of snow cover and precipitation using Special Sensor Microwave/Imager. *J. Geophys. Res.*, **96,** 7423–7435.

Hinton, B. B., W. S. Olson, D. W. Martin, and B. Auvine, 1992: A passive microwave algorithm for tropical oceanic rainfall. *J. Appl. Meteor.*, **31,** 1379–1395.

Jorgensen, D. P., and M. A. LeMone, 1989: Vertical velocity characteristics of oceanic convection. *J. Atmos. Sci.*, **46,** 621–640.

Kramer, H. J., 1994: *Observation of the Earth and Its Environment. Survey of Missions and Sensors.* 2d ed. Springer–Verlag, 580 pp.

Kummerow, C., 1993: On accuracy of the Eddington approximation for radiative transfer in the microwaves frequencies. *J. Geophys. Res.*, **98,** 2757–2765.

——, and J. A. Weinman, 1988: Determining microwave brightness temperatures from precipitating horizontally finite and vertically structured clouds. *J. Geophys. Res.*, **93,** 3720–3728.

——, and L. Giglio, 1994a: A passive microwave technique for estimating rainfall and vertical structure information from space. Part I: Algorithm description. *J. Appl. Meteor.*, **33,** 3–18.

——, and ——, 1994b: A passive microwave technique for estimating rainfall and vertical structure information from space. Part II: Application to SSM/I data. *J. Appl. Meteor.*, **33,** 19–34.

——, W. S. Olson, and L. Giglio, 1996: A simplified scheme for obtaining precipitation and vertical hydrometeor profiles from passive microwave sensors. *IEEE Trans. Geosci. Remote Sens.*, **34,** 1213–1232.

LeMone, M. A., and E. J. Zipser, 1980: Cumulonimbus vertical velocity events in GATE. Part I: Diameter, intensity, and mass flux. *J. Atmos. Sci.*, **37,** 2444–2457.

Liu, G., and J. A. Curry, 1992: Retrieval of precipitation from satellite microwave measurement using both emission and scattering. *J. Geophys. Res.*, **97,** 9959–9974.

Marecal, V., T. Tani, P. Amayenc, C. Klapisz, E. Obligis, and N. Viltard, 1997: Rain relations inferred from microphysical data in TOGA COARE and their use to test a rain profiling method from radar measurements at K_u-band. *J. Appl. Meteor.*, **36,** 1629–1646.

Marshall, J. S., and W. M. Palmer, 1948: The distribution of raindrops with size. *J. Meteor.*, **5,** 165–166.

Marzoug, M., and P. Amayenc, 1994: A class of single- and dual-

frequency algorithms for rain-rate profiling from a spaceborne radar. Part I: Principles and tests from numerical simulations. *J. Atmos. Oceanic. Technol.,* **11,** 1480–1506.

McFarquhar, G. M., and A. J. Heymsfield, 1996: Microphysical characteristics of three anvils sampled during the central equatorial Pacific experiments. *J. Atmos. Sci.,* **53,** 2401–2423.

McGaughey, G., and E. J. Zipser, 1996: Passive microwave observations of the stratiform regions of two tropical oceanic mesoscale convective systems. *J. Appl. Meteor.,* **35,** 1949–1962.

——, E. J. Zipser, R. W. Spencer, and R. E. Hood, 1996: High-resolution passive microwave observations of convective systems over the tropical Pacific Ocean. *J. Appl. Meteor.,* **35,** 1921–1947.

Mugnai, A., E. A. Smith, and G. J. Tripoli, 1993: Foundations for statistical–physical precipitation retrieval from passive microwave satellite measurements. Part II: Emission-source and generalized weighting-function properties of a time-dependent cloud-radiation model. *J. Appl. Meteor.,* **32,** 17–39.

Obligis, E., and C. Klapisz, 1996: Microwave scattering by nonspherical and inhomogeneous hydrometeors. Simulations, observations and retrievals during the TOGA COARE experiment. *Proc. Sensors and Propagation Panel Symp.,* Toulouse, France, AGARD.

Petty, G., and K. B. Katsaros, 1992: *Nimbus-7* SMMR precipitation observations calibrated against surface radar during TAMEX. *J. Appl. Meteor.,* **31,** 489–505.

Prabhakara, C., G. Dalu, G. L. Liberti, J. J. Nucciarone, and R. Suhasini, 1992: Rainfall estimation over oceans from SMMR and SSM/I microwave data. *J. Appl. Meteor.,* **31,** 532–552.

Roux, F., and M.-P. Moine, 1996: Heat and momentum fluxes associated with mesoscale convective systems observed during TOGA COARE. *Proc. Seventh Conf. on Mesoscale Processes,* Reading, United Kingdom, Amer Meteor. Soc., 298–300.

Simpson, J., F. Adler, and G. North, 1988: A proposed tropical rainfall measuring mission (TRMM) satellite. *Bull. Amer. Meteor. Soc.,* **69,** 278–295.

Smith, E. A., A. Mugnai, H. J. Cooper, G. J. Tripoli, and X. Xiang, 1992: Foundations for statistical–physical precipitation retrieval from passive microwave satellite measurements. Part I: Brightness-temperature properties of a time dependent cloud-radiation model. *J. Appl. Meteor.,* **31,** 506–531.

Spencer, R. W., H. M. Goodman, and R. E. Hood, 1989: Precipitation retrieval over land and ocean with the SSM/I: Identification and characteristics of the scattering signal. *J. Atmos. Oceanic Technol.,* **6,** 1553–1562.

Takahashi, T., K. Suzuki, M. Orita, M. Tokuno, and R. de la Mar, 1995: Videosonde observations of precipitation processes in equatorial cloud clusters. *J. Meteor. Soc. Japan,* **73,** 509–534.

Webster, P. J., and R. Lukas, 1992: TOGA COARE: The coupled ocean–atmosphere response experiment. *Bull. Amer. Meteor. Soc.,* **73,** 1377–1417.

Wilheit, T. T., A. T. C. Chang, and L. S. Chiu, 1991: Retrieval of monthly rainfall indices from microwave radiometric measurements using probability distribution functions. *J. Atmos. Oceanic Technol.,* **8,** 118–136.

Wu, R., and J. A. Weinman, 1984: Microwave radiances from precipitating clouds containing aspherical ice, combined phase, and liquid hydrometeors. *J. Geophys. Res.,* **89,** 7170–7178.

Zipser, E. J., and M. A. LeMone, 1980: Cumulonimbus vertical velocity events in GATE. Part II: Synthesis and model core structure. *J. Atmos. Sci.,* **37,** 2458–2469.